Quaternary Research xxx (2010) xxx–xxx

Contents lists available at ScienceDirect

Quaternary Research

journal homepage: www.elsevier.com/locate/yqres

Microscopic and environmental controls on the spacing and thickness of segregated ice lenses

Alan W. Rempel

Department of Geological Sciences, University of Oregon, Eugene, OR 97403-1272

ARTICLE INFO

Article history:
Received 4 December 2008
Available online xxxx

Keywords:
Frost heave
Ice lens
Patterned ground
Periglacial
Premelting
Segregated ice
Permafrost
Paleoclimate

ABSTRACT

The formation of segregated ice is of fundamental importance to a broad range of permafrost and periglacial features and phenomena. Models have been developed to account for the microscopic interactions that drive water migration, and predict key macroscopic characteristics of ice lenses, such as their spacings and thicknesses. For a given set of sediment properties, the temperature difference between the growing and incipient lenses is shown here to depend primarily on the ratio between the effective stress and the temperature deviation from bulk melting at the farthest extent of pore ice. This suggests that observed spacing between ice lenses in frozen soils, or traces of lenses in soils that once contained segregated ice, might be used to constrain the combinations of effective stress and temperature gradient that were present near the time and location at which the lower lens in each pair was initiated. The thickness of each lens has the potential to contain even more information since it depends additionally on the rate of temperature change and the permeability of the sediment at the onset of freezing. However, these complicating factors make it more difficult to interpret thickness data in terms of current or former soil conditions.

Introduction

The landforms we observe today often contain information on the conditions of their genesis. Washburn (1980) used such reasoning to interpret modern and relict occurrences of permafrost features as evidence for climate change in Arctic environments. Many, if not most, of these features contain segregated ice that forms by pushing aside mineral particles as liquid water is drawn in to fill the vacated space. Much has been learned since early experiments (Taber, 1929, 1930) and field observations (Beskow, 1935) first reported on the formation of sequences of segregated ice lenses during prolonged periods of sub-freezing surface temperatures. Here, I describe how microscopic interactions at the interfaces between mineral particles, water, and ice conspire with the prevailing environmental conditions to produce macroscopic ice lenses and determine their spacing and thickness.

Our modern understanding of ice lens growth and frost heave developed along a number of fronts; a history of the early literature is given by Henry (2000). The first comprehensive and tractable model for ice lens growth was produced by O'Neill and Miller (1985). Since heat flow is normally predominantly vertical, ice lenses tend to form parallel to the ground surface and a one-dimensional treatment captures the essential controlling dynamics. Formulated as a series of differential equations that describe the conservation laws beneath the lowermost growing, or *active* lens, O'Neill and Miller's "rigid ice" model postulates the existence of a partially "frozen fringe," within which the overlying weight is supported by a mixture of ice, liquid water, and mineral particles (see Fig. 1). Water is drawn upwards through the fringe to supply lens growth, and the hydraulic requirements on fluid flow determine the distribution of fluid pressure over the ice surface. This pressure distribution produces an effective fluid force that is balanced at a given depth by the combined effects of gravity, the forces transmitted between the particles at that depth, and the forces transmitted by the ice to the particles at lower depths. Steady lens growth can occur when the water is supplied just quickly enough to enable the rate of lens growth to be matched by the rate at which the isotherms advance relative to the ground surface as heat is conducted upwards. When the flow of heat is too rapid, however, insufficient water can be drawn to the growing lens. This causes the fringe to get thicker with time as the isotherms penetrate deeper beneath the lens. Under one range of controlling parameters, fringe thickening continues indefinitely and water simply freezes within the pore space without significant lens growth. The more interesting "secondary heaving" regime is attained when all the ice beneath a particular level within the fringe is able to transmit a force to the mineral grains at lower levels that is just large enough to balance the sum of the overlying weight and the effective fluid force. Since no net force is left to push the mineral particles together when this happens, this marks the location at which a new lens is initiated in O'Neill and Miller's (1985) model. Though typically neglected, this lens-initiation condition can be generalized to address cases where soil cohesion is important. (For further discussion of the conditions

E-mail address: rempel@uoregon.edu.

0033-5894/$ – see front matter © 2010 Published by Elsevier Inc. on behalf of University of Washington.
doi:10.1016/j.yqres.2010.07.005

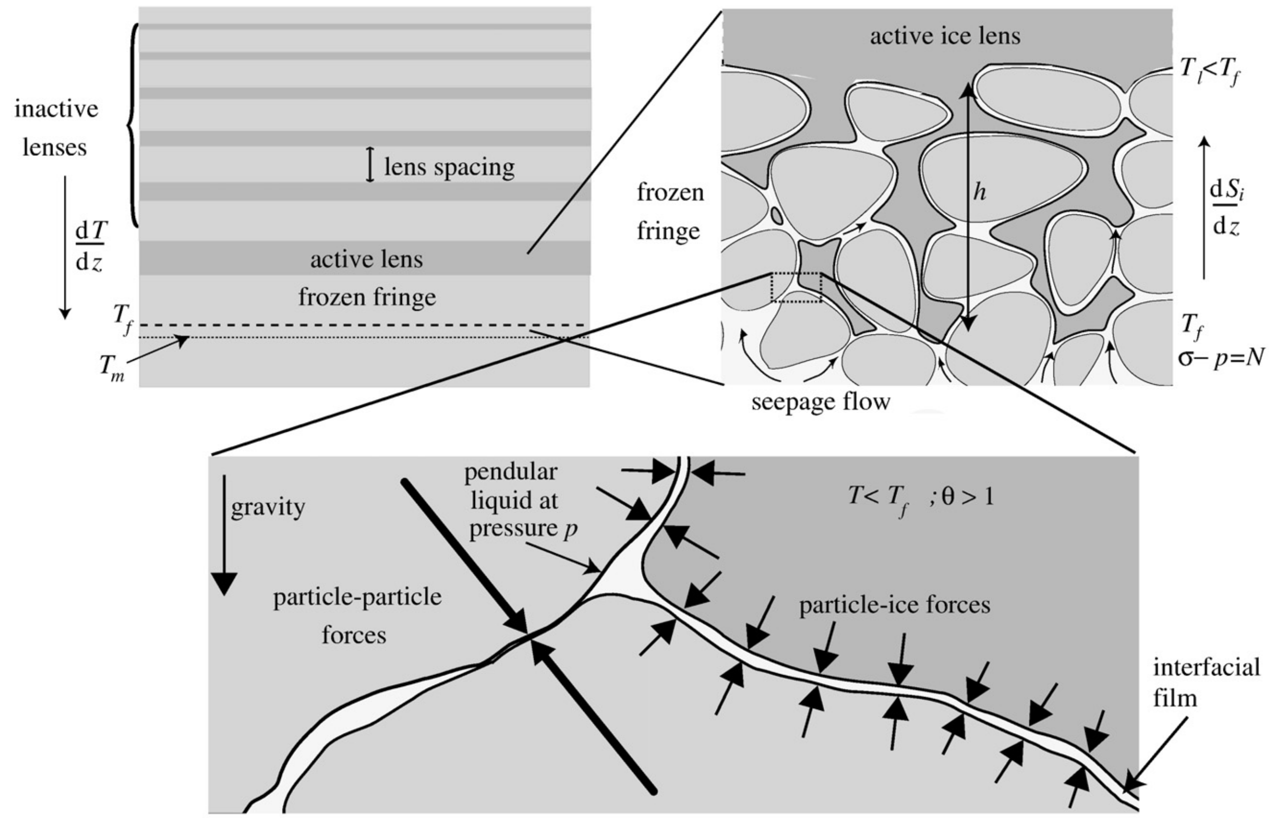

Figure 1. Schematic diagrams (not to scale) showing progressively more magnified views of a porous medium undergoing segregated ice growth; relevant dimensions are illustrated using double arrows. Important dimensional temperatures T and the corresponding reduced temperatures θ are noted on the diagrams and discussed further in the text. The effective stress N corresponds to the difference between the overburden σ and the liquid pressure p at the furthest extent of pore ice where $T=T_f$ and $\theta=1$; the ice saturation S_i in the pore space above increases in the upwards direction z.

that set the boundaries between these different freezing regimes, see Rempel et al., 2004; Rempel, 2007.)

The O'Neill and Miller (1985) model has served as the starting point for subsequent studies that have significantly improved its implementation and facilitated predictions for ice lensing behavior (e.g., Fowler, 1989; Fowler and Krantz, 1994). However, it is only quite recently that an understanding has been developed for the micro-physical controls on how forces are transmitted between the ice and the mineral particles across the thin liquid films that separate them. As discussed further below (see also Rempel et al., 2001), the net ice-particle force within the fringe is proportional to the mass of ice that would otherwise occupy the volume contained by the water and sediment, and the temperature gradient (more accurately, the gradient in chemical potential, but this and ∇T are directly related under typical freezing conditions). In the original O'Neill and Miller (1985) model the transmission of forces by the ice to underlying mineral grains had to be prescribed in an ad hoc manner. By showing that the forces acting over the ice surface can be determined without detailed knowledge of its precise geometry it has now become possible to calculate this force transmission directly (e.g., Rempel et al., 2004; Rempel, 2007). This advance makes only minor differences to predictions for the rate of lens growth (e.g., see Rempel et al., 2007), but it is crucial for enabling predictions of the conditions under which new ice lenses are initiated. This makes it possible to predict the lens spacing and thickness under varying environmental conditions.

The next section begins with a brief description of the micro-physical interactions that are ultimately responsible for the ice-particle forces that drive segregated growth. This is followed by a description of the model for ice lens initiation and growth. Particular attention is paid to the environmental controls on lens spacing and thickness—the primary potential indicators for the conditions that prevailed during ice emplacement. Post-emplacement changes can affect the observed ice distribution. These and other potential complications are discussed before the concluding remarks.

Equilibrium between ice and water at subzero temperatures

Even without any soluble impurities, two distinct sets of physical processes combine to let liquid water and ice remain in equilibrium at sub-zero temperatures (e.g., Cahn et al., 1992; Dash et al., 2006). Both phenomena have analogues above 0 °C that are described in introductory hydrogeology and geotechnical engineering textbooks. Their influence on freezing dynamics is outlined briefly here.

The surface energy of curved ice–liquid interfaces plays a role that is similar to that played by the surface tension of liquid–vapor interfaces. Under warmer conditions, surface tension enables liquid to hang above the water table within pendular rings at sub-atmospheric pressures. The curvature of the liquid–vapor interface can attain a value such that the liquid pressure is in equilibrium with the vapor concentration of the air immediately adjacent to it. At colder temperatures with the air replaced by ice, a similar liquid interface geometry is found above the lowest extent of pore ice because the energy required to maintain small liquid volumes at sub-zero temperatures is less than the surface energy that would be required for the ice surface to conform more closely to the geometry of the particles near their contacts. As the temperature cools, the ice penetrates increasingly further into confined regions and causes the liquid volumes in pendular rings to shrink (labeled as "pendular

Please cite this article as: Rempel, A.W., Microscopic and environmental controls on the spacing and thickness of segregated ice lenses, Quat. Res. (2010), doi:10.1016/j.yqres.2010.07.005

liquid" in Fig. 1). Interestingly, except for the small displacements required by the density contrast, this change in liquid fraction can be accommodated by freezing rather than by water transport (for further discussion, see Worster and Wettlaufer, 2006). The water present because of surface energy is nevertheless important for determining the permeability to fluid flow through the frozen fringe.

Surface energy effects only cause liquid water to be present at subzero temperatures where the ice interface is convex outwards. At subzero temperatures along flat interfaces, and notably along the predominantly concave interfaces that separate the ice lens from the particles that lie directly beneath, a different physical mechanism is required to allow liquid water and ice to coexist. The phenomenon known as *interfacial premelting* is crucial for causing thin films to separate the ice and particle surfaces (see Fig. 1) and enable the liquid transport that is needed along an ice-lens surface during growth (e.g., Dash et al., 2006; Rempel et al., 2004). The long-range intermolecular forces that act between the ice, the water, and the mineral surfaces are analogous to those that produce the swelling of some clays and the rich variety of other colloidal interactions that occur within groundwater flows. Interfacial premelting occurs when these long-ranged intermolecular forces (e.g., van der Waals forces, double-layer forces) are made less energetic by the insertion of a liquid layer to separate the ice and mineral surfaces. Effectively, ice is "wetted" by its own melt.

The controls on interfacial premelting are shown schematically in Figure 2. The interfacial contribution to the total free energy is represented by a dashed curve that decreases with film thickness d. At larger separations, the interfacial energy $I(d)$ trends downwards towards a limit that equates with the combined surface energies of the ice–liquid γ_{il} and the liquid–particle γ_{lp} interfaces. This sum would be the total interfacial energy if the particle and ice were pulled far enough apart (e.g., microns) that intermolecular forces between them were ineffective. At smaller separations, the interfacial energy increases towards the limiting value that would be attained with the ice and particle in direct contact γ_{ip}. It is commonly observed that most mineral surfaces are wetted by water in preference to air; similarly, particle surfaces are wetted by water in preference to ice when $\gamma_{ip} > \gamma_{il} + \gamma_{lp}$. A detailed analysis of the interfacial interactions reveals that there are circumstances under which the wetting behavior is incomplete, meaning that melt films are stable only as long as they exceed a threshold thickness, but the films disappear abruptly upon cooling below a particular temperature (e.g., Benatov and Wettlaufer, 2004; Dash et al., 2006; Hansen-Goos and Wettlaufer, 2010). The precise form of $I(d)$ turns out to be of little importance to the larger-scale heaving behavior as long as $I(d)$ decreases with d at temperatures near T_m.

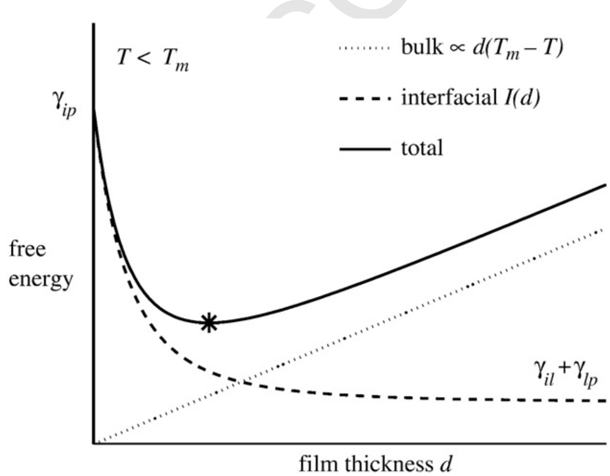

Figure 2. Schematic diagram showing the bulk (linearly increasing) and interfacial (monotonically decreasing) contributions to the free energy in an ice-particle system. The total free energy is minimized at the equilibrium film thickness shown by the asterisk.

The total free energy encompasses both interfacial and bulk contributions. The free energies of the liquid and solid phases are equal at the normal melting temperature T_m. At any subzero temperature T, however, the free energy of liquid water is greater than that of solid ice. Accordingly, the dotted line in Figure 2 shows the increase in bulk free energy that is associated with increasing the thickness of liquid. The rate of increase rises as T falls further below T_m, so the slope of the dotted line is proportional to $T_m - T$. The equilibrium configuration is reached when the total free energy is at its lowest and a small change in film thickness would cause gains and losses to the bulk and interfacial contributions that exactly offset each other. This happens at the film thickness marked by the asterisk where the slopes of the dashed and dotted curves are equal in magnitude and opposite in sign so that

$$p_\mathrm{T}(d) \equiv -I'(d) = \rho \mathcal{L} \frac{T_\mathrm{m} - T}{T_\mathrm{m}}, \tag{1}$$

where $\rho\mathcal{L} \approx 3.1 \times 10^8$ Pa is the latent heat of fusion per unit volume (note: 1 Pa $=$ 1 J/m^3), and $T_\mathrm{m} \approx 273$°K is the absolute melting temperature (a derivation is given towards the end of section 3 in Worster and Wettlaufer, 2006). Importantly, since the strengths of the intermolecular interactions that give rise to $I(d)$ decrease with the thickness of the melt film, they also give rise to the net force per unit area that the ice transmits to the particle surfaces. Its magnitude is given by the gradient in the interfacial energy so that $p_\mathrm{T}(d) = -I'(d)$, which is directly proportional to the temperature depression, as described in Eq. (1).

The laboratory study of Wilen and Dash (1995) and its subsequent theoretical analysis by Wettlaufer et al. (1996) gave one of the clearest demonstrations for how the intermolecular forces described by Eq. (1) cause the deformation that produces heave. A significant complication arises in natural porous media, where the contorted geometry causes the local particle–ice forces to act in all different directions (see the lower part of Fig. 1) and the surface energy of the ice–liquid interface, with curvature $\mathcal{K}$ (i.e. $\mathcal{K} = 2/R$ for a hemispherical cap with radius R), requires that the equilibrium condition be generalized to

$$\gamma_\mathrm{il}\mathcal{K} + p_\mathrm{T}(d) = \rho \mathcal{L} \frac{T_\mathrm{m} - T}{T_\mathrm{m}}, \tag{2}$$

In the pendular rings discussed above, for example, d is large enough that $I(d) \approx \gamma_{il} + \gamma_\mathrm{ip}$ is nearly constant so that its gradient $-p_\mathrm{T}(d) \to 0$ and the second term in Eq. (2) vanishes. Elsewhere, both terms on the left side of Eq. (2) are important and their relative sizes vary from place to place along the ice surface. In principle, the net *thermomolecular* force exerted between the ice and the mineral particles across the premelted liquid film can be calculated as the integral of $p_\mathrm{T}(d)$ over the ice surface. The complicated and poorly constrained surface geometry makes such a direct calculation impractical. However, it can be shown that the integral of the curvature $\mathcal{K}$ over any closed surface is exactly zero. This implies that the net thermomolecular force can be found by integrating the right side of Eq. (2) over a judiciously chosen closed surface, or equivalently its gradient over the enclosed volume. The result is equivalent to a *thermodynamic buoyancy* force that increases with the mass of ice that would otherwise occupy the space taken up by everything else that sits on the cold side of the T_m isotherm (Rempel et al., 2001). This insight is used within the continuum description of ice lens growth and frost heave that is outlined next.

Ice segregation model

In a fully saturated, incompressible porous medium, the rate of growth of a segregated ice lens V_l is proportional to the rate of water transport. Changes in this growth rate are small enough that inertia is negligible and the forces acting on the ice lens are balanced. This implies that the integrated fluid pressure over the ice surface from the fringe base to the lens boundary exactly counteracts the effects of gravitational and thermodynamic buoyancy. Darcy's law describes how the fluid pressure gradient and rate of water transport are related through the effective permeability k and liquid viscosity $\eta\approx 1.8\times 10^{-3}$ Pa s. When the temperature at the lower side of the lens boundary drops below a threshold T_f, a frozen fringe forms beneath and the permeability in the ice-clogged sediments is reduced below its ice-free value so that $k<k_0$. The distribution of pore sizes and other geometrical characteristics determine T_f and the fraction of the pore space that is saturated with ice S_i, as well as $k(S_i)$, at any particular temperature $T<T_f$. The small density difference between water and ice makes no significant contribution to the dynamics and both are referred to here as ρ for simplicity, whereas the density of the mineral particles is referred to as ρ_p. It is convenient to calculate the thermodynamic buoyancy in terms of the reduced temperature $\theta\equiv(T_m-T)/(T_m-T_f)$. For values of $\theta>1$ the ice saturation $S_i>0$.

Since new lenses are expected to form within a partially frozen fringe that extends beneath lenses that have their lower boundary at reduced temperatures $\theta_l>1$, the focus is on this regime of ice lens growth. Mass conservation requires that the Darcy transport velocity at a given level must balance the rate of ice motion above, which is $(1-\phi S_i)V_l$, where ϕ is the porosity. Defining $g\approx 9.8$ m^2/s as the acceleration of gravity, the vertical component of the fluid force per unit area over the surface of an ice lens with $\theta_l>1$ attached to pore ice extending downwards a distance h beneath is found as

$$\eta V_l\int_1^{\theta_l}\frac{(1-\phi S_i)^2}{k}\frac{d\theta}{d\theta/dz}=p_f\left(\theta_l-\int_1^{\theta_l}\phi S_i d\theta\right)-\left[N-(1-\phi)\left(\rho_p-\rho\right)gh\right], \tag{3}$$

where z is oriented upwards towards colder temperatures and higher θ. The integral on the left represents the non-hydrostatic part of the volumetrically averaged fluid pressure gradient through the fringe; this is equal to the integral of the non-hydrostatic part of the fluid pressure, or hydrodynamic pressure, itself over the ice surface. On the right hand side the first term accounts for the thermodynamic buoyancy produced by ice–particle interactions throughout the fringe, where the pressure scale $p_f\equiv\rho\mathcal{L}(T_m-T_f)/T_m$. The second term accounts for gravitational buoyancy and is given by the difference between the effective stress N at the furthest extent of pore ice, and the buoyancy of the mineral particles throughout the depth of the fringe. With the sediment constitutive behavior parameterized by $S_i(\theta)$ and $k(\theta)$, for known $d\theta/dz$ Eq. (3) can be used to calculate how the rate of ice-lens growth V_l depends on the reduced temperature of its boundary θ_l, the underlying effective stress N, and the fringe thickness h.

The conditions for lens initiation are key to predicting the measurable characteristics of lens spacing and thickness that are sometimes preserved afterwards. At any given level within the fringe, the force per unit area transmitted between particle contacts p_p satisfies

$$\frac{dp_p}{dz}=\frac{(1-\phi S_i)^2}{k}\eta V_l-p_f\theta\frac{d(\phi S_i)}{dz}-(1-\phi)\left(\rho_p-\rho\right)g, \tag{4}$$

where z is oriented upwards and the three terms on the right describe the gradients in hydrodynamic pressure, thermodynamic buoyancy, and gravitational buoyancy. At the lowermost extent of pore ice $p_p=N$; this is a distance h beneath the lens at the level that $\theta=1$. Above this, during lens growth with $V_l>0$ the value of p_p first declines (i.e. $dp_p/dz<0$) but can reach a minimum at an intermediate level within the fringe where $dp_p/dz=0$. A new lens is expected to be initiated at the level z_n where this minimum value of p_p first reaches zero. The new lens is assumed to cut off the water supply needed for further growth of the old lens, so the spacing between lenses is set by the difference between the fringe thickness just prior to initiation and the remaining depth of fringe lying beneath z_n. The thickness of an ice lens is determined by its integrated rate of growth over its lifetime.

To illustrate the lensing behavior in more detail requires information on the manner in which ice saturation and permeability vary with reduced temperature for the particular sediment of interest. In principle, the micro-physical controls on ice–liquid equilibrium that were described in the previous section could be used to calculate how the liquid geometry depends on temperature (e.g., Cahn et al., 1992; Hansen-Goos and Wettlaufer, 2010). Natural porous media are far too complicated to make this approach practical. Fortunately, Andersland and Ladanyi (2004) have compiled empirical freezing data for a range of porous media types, mainly silts and clays, that can be represented reasonably well with parameterizations of the form $S_i\approx 1-\theta^{-\beta}$ and $k\approx k_0\theta^{-\alpha}$, for constant values of α and β. For simplicity, consider the case where the reduced temperature through the fringe can be approximated as $\theta=1+Gz$, where $G=(-dT/dz)/(T_m-T_f)$ is a scaled representative temperature gradient that is treated as constant (the effects of nonlinearities in dT/dz will be discussed further below). Under these conditions an analytical expression for the dependence of the lens growth rate V_l on its thickness h or bounding reduced temperature $\theta_l=1+Gh$ can be found from Eq. (3), and Eq. (4) can be solved analytically for the force per unit area p_p exerted between particle contacts within the fringe. Of interest for determining the lens spacing are the locations at which new lenses are initiated and the thickness of the fringe when this occurs. For the case considered here, the particle contacts are first unloaded (i.e., $p_p=0$, and $dp_p/dz=0$) at a location z_n and reduced temperature $\theta_n=1+Gz_n$ that satisfies

$$\frac{N}{p_f}=\frac{\phi\beta}{1-\beta}\left(\theta_n^{1-\beta}-1\right)+\nu(\theta_n-1)-\frac{\Gamma_1(\theta_n)}{\Gamma_2(\theta_n)}\left(\phi\beta\theta_n^{-\beta}+\nu\right), \tag{5}$$

where the buoyancy ratio $\nu\equiv(1-\phi)(\rho_p-\rho)g/(p_fG)=(1-\phi)(\rho_p-\rho)gT_m/(-\rho\mathcal{L}dT/dz)$ measures the relative importance of gravitational and thermodynamic buoyancy forces on the particles in the fringe, and the functions $\Gamma_1(\theta)$ and $\Gamma_2(\theta)$ are defined as

$$\begin{aligned}\Gamma_1(\theta)&\equiv\int_1^{\theta}\frac{(1-\phi S_i)^2}{k/k_0}d\theta\\&=\frac{(1-\phi)^2}{1+\alpha}\left(\theta^{1+\alpha}-1\right)+\frac{2\phi(1-\phi)}{1+\alpha-\beta}\left(\theta^{1+\alpha-\beta}-1\right)\\&\quad+\frac{\phi^2}{1+\alpha-2\beta}\left(\theta^{1+\alpha-2\beta}-1\right),\\ \Gamma_2(\theta)&\equiv\frac{(1-\phi S_i)^2}{k/k_0}=(1-\phi)^2\theta^{\alpha}+2\phi(1-\phi)\theta^{\alpha-\beta}+\phi^2\theta^{\alpha-2\beta};\end{aligned}$$

Figure 3 illustrates the behavior of these functions for the case of Chena silt. The thickness h^* and reduced temperature $\theta_l^*=1+Gh^*$ of the fringe when the new lens is inititated satisfy

$$\frac{N}{p_f}=\theta_l^*(1-\phi)+\frac{\phi}{1-\beta}\left(\theta_l^{*(1-\beta)}-\beta\right)+\nu(\theta_l^*-1)-\frac{\Gamma_1(\theta_l^*)}{\Gamma_2(\theta_n)}\left(\phi\beta\theta_n^{-\beta}+\nu\right). \tag{6}$$

Lens spacing

Together, Eqs. (5) and (6) predict the spacing between lenses (or thickness of intervening frozen sediment layers, see Fig. 1) as $l_s\equiv h^*-z_n=(\theta_l^*-\theta_n)/G$. Alongside the temperature gradient, the other important environmental parameter controlling l_s is the effective stress N. In Figure 4 plots of Gl_s are shown as a function of N/p_f for several different values of the buoyancy ratio ν, which is expected to typically be small and play a comparatively minor role during sub-aerial freezing. Note that G^{-1} is

Please cite this article as: Rempel, A.W., Microscopic and environmental controls on the spacing and thickness of segregated ice lenses, Quat. Res. (2010), doi:10.1016/j.yqres.2010.07.005

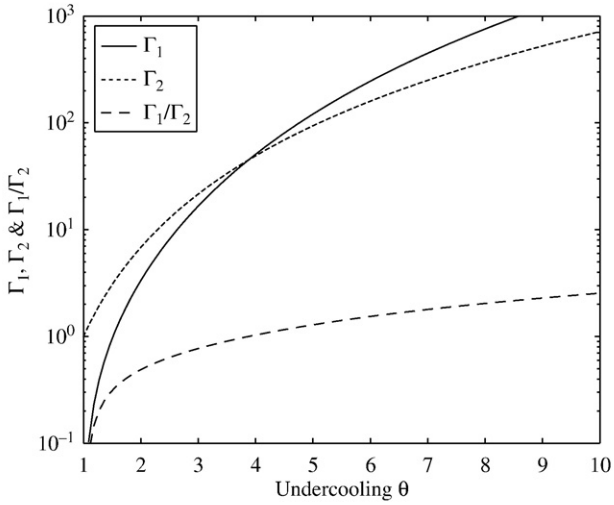

Figure 3. The functions $\Gamma_1(\theta)$ (solid) and $\Gamma_2(\theta)$ (dashed) used to account for the effects that ice saturation and permeability variations have on liquid flow through the fringe - calculated here using the parameters for Chena silt ($\alpha=3.1$, $\beta=0.53$, $\phi=0.35$). The ratio Γ_1/Γ_2 that appears in Eq. (5) is also shown (dot-dashed).

equal to the distance over which the temperature changes by the characteristic amount T_m-T_f; from this it follows that Gl_s marks the number of times by which the lens spacing exceeds this characteristic distance. Not surprisingly, the scaled spacing between lenses Gl_s is found to increase with N/p_f. The precise form of the dependence shown in Figure 4 is also influenced by the porosity ϕ and the exponents α and β that describe the constitutive behavior of the sediments; the role played by these parameters is illustrated in Figure 6 and will be discussed later. Interestingly, it turns out that the lens spacing that is predicted from these calculations has no direct dependance on the ice-free permeability k_0, which is typically one of the more uncertain parameters in the natural physical system.

For a quantitative example, consider the case where the liquid pressure at the base of the fringe and the weight of overlying material are both proportional to the depth below the ground surface H so that $N\approx(\rho_b-\rho)gH$, where ρ_b is the average density of material above the fringe base. For example if the total heave, or thickness of overlying lenses, is much less than H then $\rho_b\approx(1-\phi)\rho_p+\phi\rho$. In such circumstances $N/p_f\approx(\rho_b/\rho-1)gHT_m/[\mathcal{L}(T_m-T_f)]\approx\left(8.1\times10^{-3}\right)H/(T_m-T_f)^\circ\mathrm{C/m}$ when $\rho_b\approx2.0\rho$. The scaled fringe thickness is $Gl_s=|dT/dz|l_s/(T_m-T_f)$, which shares the same inverse dependence on the temperature scale T_m-T_f. Using the freezing parameters of Chena silt (Andersland and Ladanyi, 2004) to illustrate the predicted behavior, with $T_m-T_f\approx0.031^\circ\mathrm{C}$ this implies that $N/p_f\approx0.26H\ \mathrm{m}^{-1}$ and the asterisk at $N/p_f=0.026$ in Figure 4 shows that $Gl_s\approx2.8$ when $H=0.1$m, whereas the plus sign at $N/p_f=0.26$ indicates that $Gl_s\approx9.0$ when $H=1$m (and $\nu\rightarrow0$). Multiplying by T_m-T_f, at these depths the predicted temperature differences between the incipient and old lenses are $|dT/dz|l_s\approx0.09^\circ$C and 0.3 °C for H = 0.1 and 1 m, respectively. These predicted temperature differences depend primarily on the effective stress N and the temperature scale T_m-T_f that is a characteristic of the sediment freezing behavior. The predicted lens spacing is inversely related to the temperature gradient. For $|dT/dz|\approx10^\circ$C/m the predicted lens spacing at H = 0.1 m is $l_s\approx0.009$ m and $l_s\approx0.03$ m at H = 1 m. The temperature gradient is typically expected to decrease with H and this would tend to cause a more rapid increase in l_s with freezing depth. This example illustrates the predicted behavior in a loading regime where the temperature gradient has a stronger influence on the lens spacing than does the overlying material weight. This is true of comparatively low values where the rate of increase of Gl_s with N/p_f is comparatively slow, whereas Figure 4 indicates that at higher values Gl_s is much more sensitive to N/p_f. The asymptotic behavior predicted by Eqs. (5) and (6) for large values of θ_n and θ_l^* and $\nu=0$ has

$$Gl_s\approx\left[\frac{(1-\phi)(1+\alpha)\theta_n^{\alpha+\beta}}{\phi\beta}\right]^{1/\alpha}-\theta_n,\ \text{where}\ \theta_n\approx\left[\frac{N}{p_f}\frac{(1-\beta)(1+\alpha)}{\phi\beta(\alpha+\beta)}\right]^{1/(1-\beta)}.$$

The focus in much of the frost heave literature has been on determining heave rates for different sediments as a function of imposed surface conditions. Unfortunately, published results from frost heave experiments rarely include sufficient information for a quantitative test of the predictions of this simple model for the spacings between ice lenses. Qualitative comparisons can, however, be made for some cases. In a typical configuration, imposed loads at the sediment surface are much larger than the increase in sediment overburden over the duration of a single experiment so that N/p_f is kept approximately constant. For example, the experiment illustrated in Figure 2 of Taber (1930) (reproduced in Fig. 2 of Rempel et al., 2004 and Fig. 1 of Rempel, 2007) shows a sequence of lenses formed in a clay cylinder that was cooled from above. The spacing between the lower-most pair of lenses is approximately 1.1 cm, whereas the pair immediately above are separated by 1.0 cm, the pair above those by 0.8 cm, and the next by 0.7 cm. The observed gradual increase in lens spacing with depth is consistent with the expectation for the reported experimental procedure, wherein the temperature gradient through the fringe is inferred to have decreased as time progressed. To quantify this change in temperature gradient requires knowledge of the sediment constitutive behavior and the effective stress. For example, setting $\phi=0.35$, $\alpha=3.1$, $\beta=0.53$, and assigning $p_f=2\times10^5$ Pa, as a typical value for a clay (see e.g., Andersland and Ladanyi, 2004), with $N\approx0.25p_f$ so that $Gl_s\approx9$ from Figure 4, the temperature gradients inferred for the measured values of l_s reported above decrease from 2.3 to 2.0 to 1.6 to 1.5°C/cm during the intervals when each successive lens was emplaced (the assumed effective stress was chosen to be roughly consistent with the reported heave rate when Eq. (7) below is used for the rate of lens growth).

Temperature gradient estimates should require fewer assumptions in field settings where the depth below the ground surface is known so that the effective stress can be estimated and the constitutive behavior of the soil can be determined from measurements on recovered samples. With N/p_f known, Gl_s can be taken from Figure 4 or calculated using Eqs. (5) and (6), and upon dividing by the measured lens spacings one obtains $G=(-dT/dz)/(T_m-T_f)$. In some cases it may even be possible to infer past lens spacings long after the ice itself has melted away by measuring the separation between observed partings in the soil (known as platy soil structure, Bernard Hallet, personal communication). The inferred temperature gradients obtained in this way might be used to test scenarios for the environmental forcing at a particular location; for example, higher temperature gradients at a given depth can be interpreted to imply a greater heat flux from the ground surface and a more abrupt onset of freezing, as would be expected to accompany colder temperatures.

Lens thickness

The lens thickness l_t depends on the rate of freezing and the integrated history of lens growth, so l_t is sensitive to k_0. For the same ice saturation and permeability functions as those used above, Eq. (3) predicts that the lens growth rate satisfies

$$V_l=\frac{V}{\Gamma_1(\theta_l)}\left[\theta_l(1-\phi)+\frac{\phi}{1-\beta}\left(\theta_l^{1-\beta}-\beta\right)-\frac{N}{p_f}+\nu(\theta_l-1)\right],\qquad(7)$$

where the characteristic velocity scale is defined as $V\equiv k_0p_fG/\eta=k_0\rho\mathcal{L}|dT/dz|/(\eta T_m)$. The lens thickness depends on how much growth can occur during the time taken for its reduced temperature to evolve from θ_n to θ_l^* as the isotherms penetrate progressively deeper. This suggests that the lens thickness can be predicted as

$$l_t = \int_{\theta_n}^{\theta_l^*} \frac{V_l}{\dot{\theta}_l} d\theta_l, \tag{8}$$

where $\dot{\theta}_l \equiv d\theta_l / dt$ is determined by the transport of latent and sensible heat. For simplicity, consider the case where the duration of lens growth is short in comparison with the time over which $\dot{\theta}_l$ undergoes significant change. This is expected to be the case when the heat flux towards the ground surface at depth H greatly exceeds the latent heat $\rho \mathcal{L} V_l$ required for the lens and fringe ice to grow. Figure 5 shows the scaled lens thickness that is predicted to result, plotted as a function of N/p_f for the same parameter choices used to generate the predictions for scaled lens spacing shown in Figure 4. At higher levels of N/p_f, the increased lens spacing shown in Figure 4 indicates that lens growth occurs over a broader temperature range. However, since the temperature needs to be colder at lens initiation in order to support larger gravitational loads, the initial fringe thickness increases with N/p_f and the rate of water supply is increasingly restricted by the ice-clogged pores. This has the effect of reducing the initial rate of lens growth $V_l(\theta_n)$ and the integrated result predicted by Eq. (8) is a decrease in l_t with N/p_f, as shown in Figure 5.

For a quantitative illustration, using the behavior of Chena silt again and the simple dependence of N on depth described above, with $H = 0.1$m so that $N/p_f \approx 0.026$, the asterisk in Figure 5 indicates that $l_t \dot{\theta}_l / V \approx 1.1$, whereas the plus sign marks a value of $l_t \dot{\theta}_l / V \approx 0.14$ when the depth H and N/p_f are increased tenfold. The unfrozen permeability of Chena silt is $k_0 \approx 4.1 \times 10^{-17}$m^2 (Andersland and Ladanyi, 2004) so the velocity scale $V \approx 2.5 \times 10^{-8} dT/dzm^2/(°C\ s)$. Estimates for both the temperature gradient and the rate of change of reduced temperature at the lens boundary are needed to predict l_t. Note that $\dot{\theta}_l = -(T_m - T_f)^{-1} dT_l/dt$ so that with $T_m - T_f \approx 0.031$ °C and the lens temperature decreasing at a rate of 1 °C per day (1.2×10^{-5}°C/s) the rate of change of reduced temperature is $\dot{\theta}_l \approx 3.7 \times 10^{-4} s^{-1}$. For a temperature gradient of $|dT/dz| = 10$ °C/m the predicted lens thickness at $H = 0.1$m is $l_t \approx 7.4 \times 10^{-4}$m and $l_t \approx 9.5 \times 10^{-5}$m at $H = 1$m. These calculations suggest that for the lens thickness to increase with depth as is often seen, the ratio of $|dT_l/dt|/|dT/dz|$ must increase with depth to offset the predicted decrease in $l_t \dot{\theta}_l / V$ with N/p_f that is shown in Figure 5. For example, if $|dT_l/dt|$ were to stay approximately constant as $|dT/dz|$ decreased in proportion to the freezing depth, reaching $|dT/dz| \approx 1$°C/m at $H = 1$m, these calculations predict that l_t would increase slightly from 0.74mm at $H = 0.1$m to 0.95mm at $H = 1$m. It should be recognized as well that the assumption used here of a linear increase in N with H should be used with caution since the water pressure at the fringe base in a particular field setting is governed by local hydrogeological considerations.

Experiments by Penner (1986) provide a qualitative test of predicted changes in lens thickness with experimental parameters. Using inter-layered samples of Leda clay against a mixture of Fairbanks silts, meant to represent varved sediments, Penner applied a constant imposed stress and ramped the temperatures at both ends of his samples at a controlled rate. The temperature gradient through the fringe can be estimated from the isotherms plotted in his Figure 6 as nearly constant at between 90 and 100 °C /m throughout the experimental duration. Just prior to the formation of his numbered lens 7, the rate of temperature change imposed on both sample boundaries was decreased by a factor of 5. The thickness of lens number 6 inferred from the heave accumulation reported in his Figure 5 was 0.5 mm, whereas the thickness of lens number 8 was 2.3 mm—representing an increase by a factor of 4.6. This is roughly consistent with the expected five-fold increase predicted by the current model under the assumption that the rate of change of the temperature at the lens-fringe interface is comparable to the imposed rate of change of temperature at the sample boundaries.

It should be noted that the thicknesses of the "varves" in these experiments were a controlling factor in determining lens spacing since lens nucleation tended to occur along each silt-to-clay interface. However, consistent with expectations for a cooling lens boundary with a progressively decreasing nearby permeability and increasing fringe thickness, the experimental data reported in Penner's Figure 7 shows that heave was much less rapid during the later stages of growth for each lens than the average over the lens lifetime. Therefore the thickness data is interpreted to be only weakly influenced by the varved nature of the experimental medium and hence the reported change in lens thickness following immediately upon a change in cooling rate provides qualitative support for the current model.

More accurate predictions for the lens thickness l_t under field conditions require a proper treatment of the temperature evolution through time. From a practical standpoint, such calculations are much more involved than those entered into here (e.g., Rempel, 2007), and they also require considerable knowledge or assumptions about the environmental forcing. In contrast, l_s is predicted to primarily depend on only the dimensionless load N/p_f and the scaled temperature gradient G, but not at all on the unfrozen permeability k_0 or the rate at which the lens temperature changes. In testing scenarios for past environmental forcing using temperature gradient estimates obtained from measured lens spacings, a set of measured lens thicknesses could provide a valuable additional constraint.

Discussion

The calculations shown here suggest that observations of the spacing between lenses l_s hold potential for inferring the fringe temperature gradient during lens growth. As a complicating factor, the expected lens spacing depends also on the effective stress N, and certain properties of the sediments. Figure 6 illustrates the sensitivity of l_s to a) the porosity ϕ, b) the empirical permeability exponent α (i.e. from the power law used to describe the reduction in permeability with reduced temperature $k = k_0 \theta^{-\alpha}$), and c) the ice saturation exponent β (i.e., from the power law used to describe the increase in ice saturation with reduced temperature $S_i = 1 - \theta^{-\beta}$). For any particular N/p_f, at higher porosities the fringe contains a larger volume of ice and is more effective at transmitting forces to the particles beneath a given level; this facilitates lens initiation and results in decreased lens spacing. Larger values of the permeability exponent α lead to more rapid changes in k with reduced temperature so that the liquid pressure gradient becomes steeper close to the lens boundary. Because this tends to increase the average fluid pressure nearer to the lens boundary, there is a corresponding reduction in the total force that must be transmitted by the ice to unload the sediment contacts at z_n; this also results in smaller lens spacing. Larger values of β correspond to more rapid increases in ice saturation with θ. Just prior to lens initiation, if the fringe is sufficiently thick that the rate of lens growth $V_l \to 0$, Eq. (4) describes how the gradient in p_p near the fringe base is primarily controlled by the gradient in S_i, which is higher for larger β and promotes initiation at smaller z_n. Conversely, since larger values of β tend to cause the pore space to become clogged with ice more rapidly, this leads to lower V_l for any given fringe thickness and promotes initiation at smaller h^*. Figure 6c indicates that these effects combine to give a predicted lens spacing $l_s = h^* - z_n$ that decreases with β at low N/p_f, but increases with β at high N/p_f.

The temperature scale $T_m - T_f$ is needed to translate the scaled axes in Figures 4–6 into dimensional terms. Recall that T_f represents the temperature to which pore ice can extend beneath the lens and this is limited by the curvature $\mathcal{K}$ that is needed to penetrate pores, as described by Eq. (2). Since the required $\mathcal{K}$ depends primarily on the size distribution of mineral particles, it is these geometrical details that ultimately control the value of T_f. Andersland and Ladanyi (2004) compiled data for a broad range of different sediment types, and where the specific surface area SSA was also known the data suggest a correlation of the form $T_m - T_f \approx 4.3 \times 10^{-6} [SSA/(1m^2/g)]^{2.5}$°C (see

Please cite this article as: Rempel, A.W., Microscopic and environmental controls on the spacing and thickness of segregated ice lenses, Quat. Res. (2010), doi:10.1016/j.yqres.2010.07.005

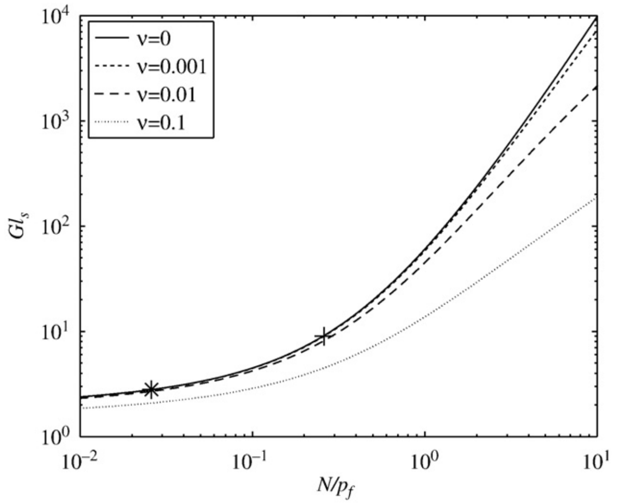

Figure 4. Scaled lens spacing $Gl_s = \theta_l^* - \theta_n$ as a function of scaled effective stress N/p_f using the parameters for Chena silt ($\alpha = 3.1$, $\beta = 0.53$, $\phi = 0.35$). The different lines correspond to calculations using different values of the fringe buoyancy parameter ν.

Fig. 3a of Rempel, 2008). Further empirical measurements of $T_m - T_f$ for the sediment types of interest in specific field settings would provide increased confidence in the validity of this fit. However, even allowing for uncertainty in the precise value of $T_m - T_f$, it is clear from the discussion above that changes in lens spacing that are observed in a given sediment can be used to infer changes in N and $|dT/dz|$.

The quantitative examples from the previous section illustrate the predicted behavior when N increases linearly with depth H. Caution should be exercised in cases where groundwater flow through low permeability, heterogeneous sediments might complicate profiles of N to such an extent that this assumption is not warranted. Even for a well-characterized sediment with known values of $T_m - T_f$, ϕ, α and β, a single set of measurements of l_s should not be viewed as sufficient to uniquely determine the values of N and dT/dz. However, a suite of such measurements does allow for the discrimination of certain combinations of N and dT/dz. Moreover, at lower values of N/p_f, the form of the curves in Figures 4 and 6 suggest that the lens spacing responds primarily to changes in the magnitude of the temperature gradient $|dT/dz|$; this diminishes the degree to which interpretations

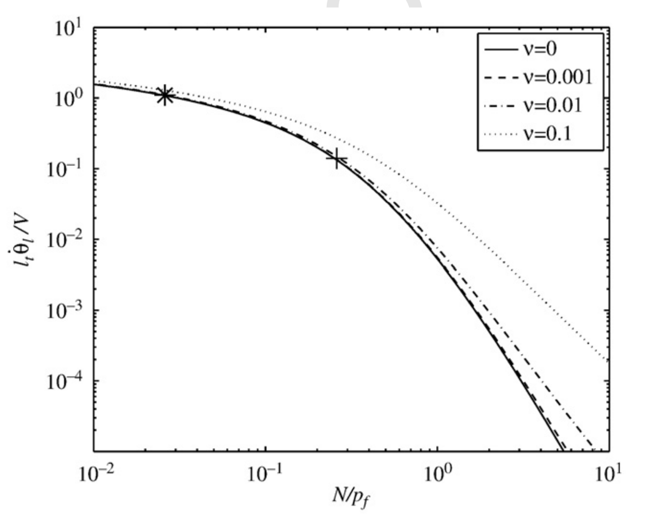

Figure 5. Scaled lens thickness $l_t\dot{\theta}_l / V$ as a function of scaled effective stress N/p_f using the parameters for Chena silt ($\alpha = 3.1$, $\beta = 0.53$, $\phi = 0.35$). The different lines correspond to calculations using different values of the fringe buoyancy parameter ν.

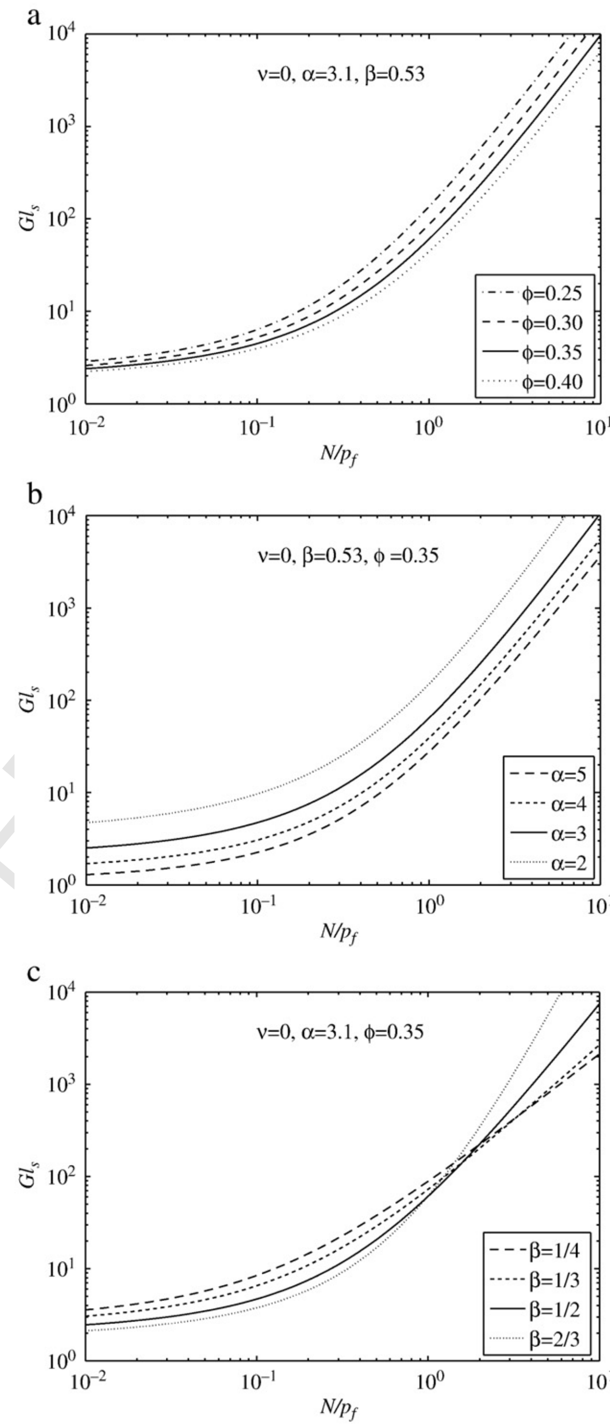

Figure 6. Scaled lens spacing $Gl_s = \theta_l^* - \theta_n$ as a function of scaled effective stress N/p_f for $\nu = 0$, and the different values of (a) ϕ, (b) α and (c) β that are noted in the legends.

of past temperature gradients can be affected by uncertainties in the past hydrologic conditions that helped to set the precise value of N.

The predictions shown here have been made while treating the temperature gradient through the fringe as constant. In actual fact, during secondary frost heave the temperature at a given location within the fringe progressively cools and this implies that S_i increases locally so that the latent heat of fusion contributes to the heat balance and causes dT/dz to vary spatially. More involved treatments that solve for the changing temperature profile within the fringe suggest that variations in dT/dz do not significantly change the essential patterns of ice growth during frost heave (e.g., Rempel, 2007). Accordingly, the temperature gradient inferred from observed l_s and assumed N/p_f represents an averaged value over the lifetime of the overlying active lens. This averaged gradient implies a local heat flux that is a combination of the conductive and latent heat fluxes through the fringe. It is perhaps worth noting that only the integral on the left side of Eq. (3) that accounts for the total hydrodynamic force on the ice surface is influenced by the details of the temperature profile through the fringe. In Eq. (4), the first two terms on the right side depend on $d\theta/dz$.

The model for lens growth presented here is based on the "rigid-ice" model of O'Neill and Miller (1985) and assumes that lenses initiate within ice that is connected through the frozen fringe to the active lens. Recent experimental and theoretical results point to additional lens initiation mechanisms that should also be considered. With a series of freezing experiments using colloidal particles of varying initial concentration, Peppin et al. (2006, 2007, 2008) demonstrated that the interaction of the freezing front with the particles causes local compaction that depresses the melting temperature where the particle volume fraction is high. This can lead to a rich variety of solidification morphologies that include dendritic and polygonal crack-like growth forms in addition to lenses. The model described above does not account for the effects of compaction, though this could done by treating the porosity as dependent on p_p within the fringe.

The discovery of cm-scale lens-like features in the basal regions of an Antarctic ice stream have been interpreted to result from frost heave (Christoffersen and Tulaczyk, 2003). The freezing behavior described here is expected to also occur at the glacier–till interface. It should be noted that the effective stresses beneath glaciers that are at their melting temperatures are typically only around one atmosphere or so—even beneath hundreds or thousands of meters of ice (Rempel, 2008).

The main difference between conditions in subglacial environments and those that pertain closer to the ground surface is not the value of N/p_f, but instead the value of the buoyancy ratio ν, which can be close to unity in the subglacial case because of the very shallow temperature gradients. Since these temperature gradients are normally only a few hundredths of a degree per meter, it is extremely unlikely that the cm-scale lens-like features that are observed are formed by the same mechanism as discussed here and originally envisioned by O'Neill and Miller (1985). (For example, taking the scaled lens spacing of $Gl_s \approx 2.8$ marked by the asterisk in Figure 4 and assuming a typical geothermal heat flux for West Antarctica of $k|dT/dz| \approx 0.08$ W/m^2, the temperature gradient is only about $|dT/dz| \approx 0.02$°C/m when the thermal conductivity is $k = 4$W/(m °C) so the predicted lens spacing would be $l_s \approx 4$m beneath a glacier that is flowing over sediment with a pore-size distribution similar to Chena silt with $T_m - T_f \approx 0.031$ °C. Nevertheless, such features appear to be reasonably common in subglacial sediments and their origin is of potential interest to glacier behavior. The sediment concentrations in these layers are sometimes lower than would be expected from random closed packing of intact particle layers and this suggests the possibility of post-entrainment particle rearrangements.

The focus in this work has been on freezing behavior and lens characteristics in unconsolidated porous media. Much of the frost damage that occurs in rocks and other cohesive materials can be traced to the same underlying physical mechanisms (e.g., Hallet et al., 1991; Matsuoka, 2001; Matsuoka and Murton, 2008; Murton et al., 2006; Walder and Hallet, 1985). Liquid water is drawn towards freezing centers by the liquid pressure gradients that are required to balance the ice–mineral forces that act across interfacially melted films at colder temperatures. Rather than the growth and initiation of new lenses, however, the extension of pre-existing fractures is in this case a much more important control on the extent of frost damage.

Conclusions

The segregation of ice into lenses that exclude mineral particles is a key aspect of the development of many permafrost features. At its heart, this behavior is caused by the influence of the mineral particles on the equilibrium phase behavior of water and ice. The net thermodynamic buoyancy force that results can be used as an ingredient of larger-scale models of freezing behavior to predict the initiation and growth of ice lenses. Using empirical formulations for the sediment freezing behavior, predictions can be made for how environmental controls determine the spacing and thicknesses of ice lenses. An approximate treatment demonstrates that the main controls on lens spacing are the effective stress at the furthest extent of pore ice, the temperature to which the ice extends, and the temperature gradient between that depth and the base of the overlying, active ice lens. The lens thickness depends additionally on the rate of change of lens temperature and the permeability of the ice-free sediments. This analysis suggests that observations of lens spacing hold promise for inferring the environmental conditions during ice emplacement. Observations of lens thickness are expected to be more difficult to interpret because of the greater sensitivity to parameters that are more difficult to constrain. These considerations bring to mind Washburn's observation in the concluding paragraph of his paper summarizing the use of permafrost features as evidence of climatic change (Washburn, 1980), namely that: "... permafrost evidence, despite numerous problems, appears to offer the exciting prospect of some quantitative and rather precisely limiting terrestrial temperature parameters that may not be obtainable in any other way." Whether this prospect is to be realized in the case of ice lens data has yet to be fully judged.

Acknowledgments

I thank Bernard Hallet and Ron Sletten for organizing the symposium in honor of Link Washburn and inviting me to attend. Two anonymous reviewers offered a number of comments and suggestions that helped to significantly improve this manuscript. I am grateful for their efforts and also for the careful comments and insight that Bernard demonstrated in highlighting their main points and adding several more of his own.

References

Andersland, O.B., Ladanyi, B., 2004. An Introduction to Frozen Ground Engineering. Chapman and Hall, New York.
Benatov, L., Wettlaufer, J.S., 2004. Abrupt grain boundary melting in ice. Physical Review. E: Statistical, Nonlinear, and Soft Matter Physics 70, 061606.
Beskow, G., 1935, Soil Freezing and Frost Heaving with Special Application to Roads and Railroads. The Swedish Geological Society, C, no 375, Year Book no. 3 (translated by J. Osterberg). Technological Institute, Northwestern University. Reprinted in: Historical perspectives in Frost Heave Research (ed. P. B. Black & M. J. Hardenberg). CRREL Special Report 91-23, pp. 37–157.
Cahn, J.W., Dash, J.G., Fu, H.-Y., 1992. Theory of ice premelting in monosized powders. Journal of Crystal Growth 123, 101–108.
Christoffersen, P., Tulaczyk, S., 2003. Response of subglacial sediments to basal freeze-on: 1. Theory and comparison to observations from beneath the West Antarctic Ice Sheet. Journal of Geophysical Research 108 (B4), 2222. doi:10.1029/2002JB001935.
Dash, J.G., Rempel, A.W., Wettlaufer, J.S., 2006. The physics of premelted ice and its geophysical consequences. Reviews of Modern Physics 78, 695–741.
Fowler, A.C., 1989. Secondary frost heave in freezing soils. SIAM Journal on Applied Mathematics 49, 991–1008.
Fowler, A.C., Krantz, W.B., 1994. A generalized secondary frost heave model. SIAM Journal on Applied Mathematics 54, 1650–1675.
Hallet, B., Walder, J.S., Stubbs, C.W., 1991. Weathering by segregation ice growth in microcracks at sustained sub-zero temperatures: verification from an experimental study using acoustic emissions. Permafrost and Periglacial Processes 2, 283–300.
Hansen-Goos, H., Wettlaufer, J.S., 2010. Theory of ice premelting in porous media. Physical Review. E: Statistical, Nonlinear, and Soft Matter Physics 81, 031604.
Henry, K.S., 2000. A Review of the Thermodynamics of Frost Heave. CRREL Technical Report 00–16, pp. 1–19.
Matsuoka, N., 2001. Direct observation of frost wedging in alpine bedrock. Earth Surface Processes and Landforms 26, 601–614.
Matsuoka, N., Murton, J., 2008. Frost weathering: recent advances and future directions. Permafrost and Periglacial Processes 19, 195–210.
Murton, J.B., Peterson, R., Ozouf, J.-C., 2006. Bedrock fracture by ice segregation in cold regions. Science 314, 1127–1129.
O'Neill, K., Miller, R.D., 1985. Exploration of a rigid ice model of frost heave. Water Resources Research 21, 281–296.
Penner, E., 1986. Ice lensing in layered soils. Canadian Geotechnical Journal 23, 334–340.
Peppin, S.S.L., Elliott, J.A.W., Worster, M.G., 2006. Solidification of colloidal suspensions. Journal of Fluid Mechanics 554, 147–166.

Please cite this article as: Rempel, A.W., Microscopic and environmental controls on the spacing and thickness of segregated ice lenses, Quat. Res. (2010), doi:10.1016/j.yqres.2010.07.005

Peppin, S.S.L., Worster, M.G., Wettlaufer, J.S., 2007. Morphological instability in freezing colloidal suspensions. Proceedings of the Royal Society of London. Series A: Mathematical and Physical Sciences 463, 723–733.

Peppin, S.S.L., Wettlaufer, J.S., Worster, M.G., 2008. Experimental verification of morphological instability in freezing aqueous colloidal suspensions. Physical Review Letters 100, 238301.

Rempel, A.W., 2007. The formation of ice lenses and frost heave. Journal of Geophysical Research 112, F020S21. doi:10.1029/2006JF000525.

Rempel, A.W., 2008. A theory for ice–till interactions and sediment entrainment beneath glaciers. Journal of Geophysical Research 113, F01013. doi:10.1029/2007JF000870.

Rempel, A.W., Wettlaufer, J.S., Worster, M.G., 2001. Interfacial premelting and the thermomolecular force: thermodynamic buoyancy. Physical Review Letters 87, 088501.

Rempel, A.W., Wettlaufer, J.S., Worster, M.G., 2004. Premelting dynamics in a continuum model of frost heave. Journal of Fluid Mechanics 498, 227–244.

Rempel, A.W., Wettlaufer, J.S., Worster, M.G., 2007. Comment on “A quantitative framework for interpretation of basal ice facies formed by ice accretion over subglacial sediment” by Poul Christoffersen et al. Journal of Geophysical Research 112, F02036. doi:10.1029/2006JF000701.

Taber, S., 1929. Frost heaving. Journal of Geology 37, 428–461.

Taber, S., 1930. The mechanics of frost heaving. Journal of Geology 38, 303–317.

Walder, J., Hallet, B., 1985. A theoretical model of the fracture of rock during freezing. Geological Society of America Bulletin 96, 336–346.

Washburn, A.L., 1980. Permafrost features as evidence of climatic-change. Earth Science Review 15, 327–402.

Wettlaufer, J.S., Worster, M.G., Wilen, L.A., Dash, J.G., 1996. A theory of premelting dynamics for all power law forces. Physical Review Letters 76, 3602–3605.

Wilen, L.A., Dash, J.G., 1995. Frost heave dynamics at a single-crystal interface. Physical Review Letters 74, 5076–5079.

Worster, M.G., Wettlaufer, J.S., 2006. Premelting dynamics. Annual Review of Fluid Mechanics 38, 427–452.